Figure 1:

Table 1: Phenotypic features of T cell activation

Figure 2:

Figure 3:

Figure 4:

Figure 5:

Supplementary Information Appendix: Architecture of a minimal signalling pathway explains the T cell response to a 1,000,000-fold variation in antigen affinity and dose

Melissa Lever[†*], Hong-Sheng Lim[†*], Philipp Kruger[†*], John Nguyen[†], Nicola Trendel[†], Enas Abu-Shah[†], Philip K. Maini[‡], P. Anton van der Merwe[†], Omer Dushek[†,‡,¶]

[†]Sir William Dunn School of Pathology, University of Oxford, Oxford, United Kingdom
[‡]Wolfson Centre for Mathematical Biology, Mathematical Institute, University of Oxford, Oxford, United Kingdom
[*]These authors contributed equally
[¶]Corresponding author

Supplementary Text

Phenotypic model equations (KPL-IFF)

The ordinary-differential-equations (ODEs) corresponding to kinetic proofreading with limited signalling coupled to incoherent feedforward (KPL-IFF, Figure 3d) are,

$$\begin{aligned}
\mathrm{d}L/\mathrm{d}t &= -k_{\text{on}}LR + k_{\text{off}}(C_0 + C_1 + C_2) \\
\mathrm{d}R/\mathrm{d}t &= -k_{\text{on}}LR + k_{\text{off}}(C_0 + C_1 + C_2) \\
\mathrm{d}C_0/\mathrm{d}t &= k_{\text{on}}LR - (k_{\text{off}} + k_{\text{p}})C_0 \\
\mathrm{d}C_1/\mathrm{d}t &= k_{\text{p}}C_0 - (k_{\text{off}} + \phi k_{\text{p}})C_1 \\
\mathrm{d}C_2/\mathrm{d}t &= \phi k_{\text{p}}C_1 - k_{\text{off}}C_2 \\
\mathrm{d}Y/\mathrm{d}t &= \gamma_+^y(Y_T - Y) - \gamma_-^y Y + \lambda C_1(Y_T - Y) \\
\mathrm{d}P/\mathrm{d}t &= \gamma_+^p(P_T - P) - \gamma_-^p P + \delta Y(P_T - P) - \mu C_1 P
\end{aligned}$$

where k_{on} and k_{off} are the TCR-pMHC kinetic rate constants, k_{p} is the kinetic proofreading rate, ϕ is the limited signalling parameter, λ is the amplification parameter, μ is the inhibition parameter, and δ is the activation

parameter. We solve the system in the steady-state to obtain the following,

$$\begin{aligned}
\hat{C}_0 &= \left(\frac{k_{\text{off}}}{k_{\text{off}}+k_{\text{p}}}\right)\hat{C}_T \\
\hat{C}_1 &= \left(\frac{k_{\text{off}}}{k_{\text{off}}+k_{\text{p}}}\right)\left(\frac{k_{\text{p}}}{k_{\text{off}}+\phi k_{\text{p}}}\right)\hat{C}_T \\
\hat{C}_2 &= \left(\frac{\phi k_{\text{p}}}{k_{\text{off}}+k_{\text{p}}}\right)\left(\frac{k_{\text{p}}}{k_{\text{off}}+\phi k_{\text{p}}}\right)\hat{C}_T \\
\hat{Y} &= \frac{1+\hat{\lambda}\hat{C}_1}{1+\hat{\lambda}\hat{C}_1+\hat{\gamma}^y} \\
\hat{P} &= \frac{1+\hat{\delta}\hat{Y}}{1+\hat{\delta}\hat{Y}+\hat{\gamma}^p+\hat{\mu}\hat{C}_1}
\end{aligned}$$

with

$$\hat{C}_T = \left((L_T/R_T+1+k_{\text{off}}/k_{\text{on}}R_T)-\sqrt{(L_T/R_T+1+k_{\text{off}}/k_{\text{on}}R_T)^2-4L_T/R_T}\right)/2$$

where we have used 'hat' quantities to represent nondimensionalized concentrations and parameters: $\hat{C}_T = C_T/R_T$, $\hat{C}_0 = C_0/R_T$, $\hat{C}_1 = C_1/R_T$, $\hat{C}_2 = C_2/R_T$, $\hat{Y} = Y/Y_T$, $\hat{P} = P/P_T$, $\hat{\lambda} = \lambda R_T/\gamma_+^y$, $\hat{\gamma}^y = \gamma_-^y/\gamma_+^y$, $\hat{\delta} = \delta Y_T/\gamma_+^p$, $\hat{\gamma}^p = \gamma_-^p/\gamma_+^p$ and $\hat{\mu} = \mu R_T/\gamma_+^p$.

The model calculations in Figure 3d were generated using $k_{\text{p}} = 0.01$ s^{-1}, $\phi = 0.1$, $\hat{\gamma^p} = \hat{\gamma^y} = 500$, $k_{\text{on}}R_T = 1$, $\hat{\lambda} = 10000$, $\hat{\delta} = 5000$, and $\hat{\mu} = 50000$ with the indicated variation of L_T/R_T (x-axis) and a variation of k_{off} from 10^{-4} to 10^2 s^{-1} (coloured lines). We provide a web applet that can be used to examine the predicted dose-response from this phenotypic model for any parameter values (Applet S1).

Systematic analysis of phenotypic model network architectures

The key objective of the systematic analysis is to determine whether other models can also produce the key features that the kinetic proofreading with limited signalling coupled to incoherent feedforward (KPL-IFF) model is able to produce (Figure 3d, Table 1).

We performed two systematic analyses of phenotypic models: a simpler systematic analysis looking at 304 networks (Figure 4a) and a more complex analysis looking at 26,069 networks (Figure 4e). Given that the methodology is identical for both analyses and that the simpler analysis is nested within the more complex analysis, this section will focus on describing the more complex analysis. The methodology extends previous efforts to systematically study pre-defined network architectures that can produce specific phenotypes (1, 2).

Defining the set of network architectures. The set network architectures that we examine are defined based on the possible reactions that we consider. Each network has a receptor that can undergo kinetic proofreading with 4 steps (C_0, C_1, C_2, and C_3) and 3 additional nodes (X, Y, and P). We consider all possible networks that have 4 reaction arrows (either activating or inhibiting) between the receptor, X, Y, and P (Figure 4d). Note that every network contains the 4 kinetic proofreading states. The total number of reaction arrows is 36 and therefore the total number of networks is 58,905 (36 choose 4). Without loss of generality we identify P as the output and remove all networks where there is no connection between any of the kinetic proofreading states and P (either directly or indirectly), which reduces the number of networks to 26,069. We omit networks where X, Y, or P modulate kinetic proofreading to maintain computational feasibility. Each network contains a total of 6 free parameters; 2 kinetic proofreading parameters (k_{p} and ϕ) and 1 parameter for each of the 4 reaction arrows.

A scale-free comparison measure. The large number of networks that are to be systematically examined means that it is not feasible to manually identify (i.e. by eye) whether a specific proposed network can also produce the output of the KPL-IFF network (Figure 3d). To automate identification we constructed a quantitative measure that can compare the output of the KPL-IFF network to a specific proposed network.

First, we define four elementary numbers for any dose-response curve (Figure S4a): the value of P at the lowest concentration (W_1), the maximum value of P (W_2), the value of P at the largest concentration (W_3), and the concentration of ligand producing half-maximal response (EC_{50}). In cases where two values of EC_{50} are possible the lower value is used (i.e. to the left of the peak in a bell-shaped dose-response).

Second, we define four metrics that capture the key qualitative features of the KPL-IFF output,

$$\begin{aligned} F_1 &= W_1/W_2 \\ F_2 &= (W_3/W_2)/(W_3^*/W_2^*) \\ F_3 &= W_2/W_2^* \\ F_4 &= EC_{50}/EC_{50}^* \end{aligned}$$

where the superscript $*$ refers to the values for an index ligand, which we take to be the highest affinity ligand. These four metrics can be calculated for each ligand and plotted as a function of the ligand k_{off} value for the KPL-IFF network (Figure S4b-g). The first measure (F_1) ensures that the dose-response curve exhibits an increase. The second measure (F_2) ensures that a bell-shaped dose-response is observed. The third measure (F_3) ensures that the peak height is similar for high affinity ligands but decreases for low affinity ligands. The fourth measure (F_4) ensures that ligands of intermediate affinity are first to increase as a function of dose. The normalisation to an index ligand means that these measures are largely independent of the absolute values of L (dose) and P (response). Note that these measures rely on fold-changes and therefore are independent of the absolute scale of the response (value of P).

Lastly, we define a single measure that can compare the similarity between F_1, F_2, F_3, and F_4 (across a wide range of k_{off} values) for any specific network and the the KPL-IFF network,

$$\text{SSR} = \sum_{i=1}^{N} (F_1^i - \widehat{F}_1^i)^2 + (F_2^i - \widehat{F}_2^i)^2 + (F_3^i - \widehat{F}_3^i)^2 + (F_4^i - \widehat{F}_4^i)^2 \tag{1}$$

where the index i represents each ligand ($i = 1$ to $i = N$ ligands with $N = 12$ in our example). The values of F with a hat represent those for the KPL-IFF network whereas the non-hat values are for the specific network being tested.

In summary, the output of any proposed network are the values of P as a function of ligand concentrations for 12 ligands with different values of k_{off}. This output is used to calculate F_1, F_2, F_3, and F_4 for each ligand which can then be used to compute SSR. Proposed networks with small SSR values are more likely to be compatible with the output of the KPL-IFF network and therefore the key features.

Workflow. The workflow for the systematic analysis is shown in Figure S4h. The first step is to select one of the 26,069 networks to analyse. The next two steps aim to determine the values of the 6 model parameters that produce the smallest value of the SSR for the selected network. First, the method performs 1 million evaluations of the network where the 6 model parameters for each evaluation are randomly sampled (uniform distribution in log-space) and the SSR for each evaluation is determined. Second, the values of the 6 parameters for the 15 network evaluations that produced the smallest values of SSR (from the 1 million that were sampled) are then used as initial conditions for a non-linear optimisation algorithm (*fminsearch* in Matlab) that uses a modified simplex method to further minimize the SSR. Finally, the 6 parameter values that produced the smallest SSR (among the 15 optimised parameter values) are recorded along with the associated SSR for the network. The procedure is repeated for all 26,069 networks.

Given that the analysis relies on two steps that have a stochastic element (random parameter sampling and further optimisation) we repeated the analysis 3 times for both the simpler and complex analysis but found no difference to the results (see below) suggesting that the search algorithm had sufficient coverage of parameter space.

Results. The output of the analysis is a list of the 26,069 networks (or the 304 networks for the simpler analysis) ordered from the smallest to the largest SSR. We summarise this output in Movie S2 (or Movie S1 for the simpler analysis) where each 1 second frame corresponds to a network architecture evaluated with the 6 optimised parameter values. By examining the movies we find that 274 of the 26,069 networks in the complex analysis (or 1 of the 304 networks in the simpler analysis) are compatible with the key features as they are able to reproduce the output of the KPL-IFF network. Importantly, all 274 compatible networks contained the same underlying KPL-IFF mechanism. In many cases these more complex networks were reduced to the same KPL-IFF model shown in Figure 3d (e.g. networks 2, 4, 7 to 21, etc) whilst in other cases the incoherent feedforward exhibited indirect inhibition (e.g. networks 1, 3, 5, 6, etc) but operated in a parameter regime where inhibition saturated after activation.

Mathematical model. The systematic analysis relies on evaluating many network architectures. To do this, we have implemented a single general mathematical model that can be reduced to all 26,069 networks by setting appropriate reactions to zero.

The ordinary-differential-equations (ODEs) corresponding to the most general mathematical model are,

$$
\begin{aligned}
\mathrm{d}L/\mathrm{d}t &= -k_{\text{on}}LR + k_{\text{off}}C_T \\
\mathrm{d}R/\mathrm{d}t &= -k_{\text{on}}LR + k_{\text{off}}C_T \\
\mathrm{d}C_0/\mathrm{d}t &= k_{\text{on}}LR - (k_{\text{off}} + k_{\text{p}})C_0 \\
\mathrm{d}C_i/\mathrm{d}t &= k_{\text{p}}C_{i-1} - (k_{\text{p}} + k_{\text{off}})C_i \quad 1 \leq i < N-1 \\
\mathrm{d}C_N/\mathrm{d}t &= k_{\text{p}}C_{N-1} - (k_{\text{off}} + \phi k_{\text{p}})C_N \\
\mathrm{d}C_{N+1}/\mathrm{d}t &= \phi k_{\text{p}}C_N - k_{\text{off}}C_{N+1} \\
\mathrm{d}X/\mathrm{d}t &= \gamma^x_+(X_T - X) - \gamma^x_- X \\
&\quad +(\vec{\lambda}^x \cdot \vec{C})(X_T - X) - (\vec{\mu}^x \cdot \vec{C})X \\
&\quad +(\eta^y_+ Y + \eta^p_+ P)(X_T - X) - (\eta^y_- Y + \eta^p_- P)X \\
\mathrm{d}Y/\mathrm{d}t &= \gamma^y_+(Y_T - Y) - \gamma^y_- Y \\
&\quad +(\vec{\lambda}^y \cdot \vec{C})(Y_T - Y) - (\vec{\mu}^y \cdot \vec{C})Y \\
&\quad +(\beta^x_+ X + \beta^p_+ P)(Y_T - Y) - (\beta^x_- X + \beta^p_- P)Y \\
\mathrm{d}P/\mathrm{d}t &= \gamma^p_+(P_T - P) - \gamma^p_- P \\
&\quad +(\vec{\lambda}^p \cdot \vec{C})(P_T - P) - (\vec{\mu}^p \cdot \vec{C})P \\
&\quad +(\delta^x_+ X + \delta^y_+ Y)(P_T - P) - (\delta^x_- X + \delta^y_- Y)P
\end{aligned}
$$

where $C_T = \sum_{i=0}^{N+1} C_i$ and $\vec{\lambda}^x \cdot \vec{C}$ is the vector dot product between the parameter vector ($\vec{\lambda}^x = [\lambda^x_0, \lambda^x_1, ...\lambda^x_{N+1}]$) and the vector of complexes ($\vec{C} = [C_0, C_1, ..., C_{N-1}, C_N, C_{N+1}]$). We solve the ODE system in the steady-state

to obtain,

$$\begin{aligned} C_0 &= \alpha^0(1-\alpha)C_T \\ C_1 &= \alpha^1(1-\alpha)C_T \\ &\vdots \\ C_{N-1} &= \alpha^{(N-1)}(1-\alpha)C_T \\ C_N &= \alpha^N\left(\frac{k_{\text{off}}}{k_{\text{off}}+\phi k_{\text{p}}}\right)C_T \\ C_{N+1} &= \alpha^N\left(\frac{\phi k_{\text{p}}}{k_{\text{off}}+\phi k_{\text{p}}}\right)C_T \end{aligned}$$

where

$$\begin{aligned} \frac{C_T}{R_T} &= \left(\frac{L_T}{R_T}+1+\frac{k_{\text{off}}}{k_{\text{on}}R_T}-\sqrt{\left(\frac{L_T}{R_T}+1+\frac{k_{\text{off}}}{k_{\text{on}}R_T}\right)^2-4\frac{L_T}{R_T}}\right)/2, \\ \alpha &= \frac{k_{\text{p}}}{k_{\text{off}}+k_{\text{p}}}, \end{aligned}$$

and the equations for X, Y, and P simplify to,

$$\begin{aligned} 0 &= (1-X)-\gamma_m^x X+(\vec{\lambda}_m^x\cdot\vec{C})(1-X)-(\vec{\mu}_m^x\cdot\vec{C})X+(\alpha_{+m}^y Y+\alpha_{+m}^p P)(1-X)-(\eta_{-m}^y Y+\eta_{-m}^p P)X \\ 0 &= (1-Y)-\gamma_m^y Y+(\vec{\lambda}_m^y\cdot\vec{C})(1-Y)-(\vec{\mu}_m^y\cdot\vec{C})Y+(\beta_{+m}^x X+\beta_{+m}^p P)(1-Y)-(\beta_{-m}^x X+\beta_{-m}^p P)Y \\ 0 &= (1-P)-\gamma_m^p P+(\vec{\lambda}_m^p\cdot\vec{C})(1-P)-(\vec{\mu}_m^p\cdot\vec{C})P+(\delta_{+m}^x X+\delta_{+m}^y Y)(1-P)-(\delta_{-m}^x X+\delta_{-m}^y Y)P \end{aligned}$$

where we have nondimensionalized concentrations (R by R_T, C_i by R_T, X by X_T, Y by Y_T, and P by P_T) but retained original notation for clarity. The subscript m indicates that the parameter has been modified as a result of the nondimensionalization process: $\gamma_m^x=\gamma_-^x/\gamma_+^x$, $\gamma_m^y=\gamma_-^y/\gamma_+^y$, $\gamma_m^p=\gamma_-^p/\gamma_+^p$, $\vec{\lambda}_m^x=\vec{\lambda}^x R_T/\gamma_+^x$, $\vec{\lambda}_m^y=\vec{\lambda}^y R_T/\gamma_+^y$, $\vec{\lambda}_m^p=\vec{\lambda}^p R_T/\gamma_+^p$, $\vec{\mu}_m^x=\vec{\mu}^x R_T/\gamma_+^x$, $\vec{\mu}_m^y=\vec{\mu}^y R_T/\gamma_+^y$, $\vec{\mu}_m^p=\vec{\mu}^p R_T/\gamma_+^p$, $\eta_{+m}^y=\eta_+^y Y_T/\gamma_+^x$, $\eta_{+m}^p=\eta_+^p P_T/\gamma_+^x$, $\eta_{-m}^y=\eta_-^y Y_T/\gamma_+^x$, $\eta_{-m}^p=\eta_-^p P_T/\gamma_+^x$, $\beta_{+m}^x=\beta_+^x X_T/\gamma_+^y$, $\beta_{+m}^p=\beta_+^p P_T/\gamma_+^y$, $\beta_{-m}^x=\beta_-^x X_T/\gamma_+^y$, $\beta_{-m}^p=\beta_-^p P_T/\gamma_+^y$, $\delta_{+m}^x=\delta_+^x X_T/\gamma_+^p$, $\delta_{+m}^y=\delta_+^y Y_T/\gamma_+^p$, $\delta_{-m}^x=\delta_-^x X_T/\gamma_+^p$, and $\delta_{-m}^y=\delta_-^y Y_T/\gamma_+^p$.

In the case of the more complex analysis (4 nodes, 4 reaction arrows) the number of kinetic proofreading steps was 4 ($N=3$). The ratio of background inhibition to background activation of X, Y, and P were fixed at 500 so that without any ligand the concentrations of X, Y, and P were near zero ($\gamma_m^x=\gamma_m^y=\gamma_m^p=500$). The remaining parameters were set to 0 with the exception of k_{p}, ϕ, and 4 other parameters that defined the network architecture. The same procedure was carried out for the simpler analysis (3 nodes, 3 reaction arrows) except that the number of kinetic proofreading steps was 3 ($N=2$) and all reactions to and from X were set to zero.

The mathematical model was numerically solved using *fzero* in Matlab (Mathworks, MA), which allowed the code to be translated to C++ by the Matlab Coder toolbox. We found that the solution converged rapidly when using 0 as the initial guess.

KPL-IFF model parameters compatible with phenotypic features

To determine the set of parameters in the KPL-IFF model (λ, δ, μ, k_{p}, ϕ) compatible with the key features we utilised Approximate Bayesian Computations with Sequential Monte Carlo (ABC-SMC) (3, 4). We used the SSR (described above) as the summary statistic and terminated the algorithm when $> 10,000$ particles were found with $SSR < 1$. Distributions of the 5 parameters along with their pairwise correlations are shown in Figure S6.

Negative feedback cannot produce a bell-shaped dose-response

The systematic analysis described in the previous section (see also main text and Fig. 4) has revealed that negative feedback, although well known to produce oscillations in time, cannot produce a bell-shaped dose-response in the steady-state. In this section we provide further evidence for this numerical result by providing an intuitive explanation together with an analytical proof.

First, consider a two component negative feedback (Figure S5a) whereby P activates Y and Y in turn inhibits P. As the activator of P increases (C_1 in this example), P will increase. In order to decrease P (to produce a bell-shaped dose-response) Y needs to inhibit P more strongly at larger values of P. But a larger value of active Y (needed for stronger inhibition of P) requires larger value of active P. Therefore, P and Y are subjected to two conflicting requirements which cannot be satisfied simultaneously. It follows that a bell-shaped dose-response for P cannot be achieved in the steady-state.

In what follows we provide a mathematical proof that a bell-shaped dose-response cannot be produced with negative feedback in the steady-state. To do this, we derive an implicit expression for P and show that the first derivative cannot be zero for any positive reaction rate constants. The non-linear coupled system of ODEs for the two component negative feedback can be written as follows,

$$\frac{\mathrm{d}\hat{Y}}{\mathrm{d}t} = \frac{\eta_+^P}{1+\left(\frac{\hat{\rho}}{\hat{P}}\right)^n} + \gamma_+^Y - \left[\frac{\eta_+^P}{1+\left(\frac{\hat{\rho}}{\hat{P}}\right)^n} + \gamma_+^Y + \gamma_-^Y\right]\hat{Y} \tag{2}$$

$$\frac{\mathrm{d}\hat{P}}{\mathrm{d}t} = (\lambda\hat{C}_1 + \gamma_+^P)(1-\hat{P}) - \hat{\beta_-^Y}\hat{Y}\hat{P} - \gamma_-^P\hat{P} \tag{3}$$

where $\hat{Y}$ and $\hat{P}$ are non-dimensional ($\hat{Y} = Y/Y_T$, $\hat{P} = P/P_T$) with $\hat{\rho} = \rho/P_T$, and $\hat{\beta_-^Y} = \beta_-^Y Y_T$. Note that all reactions considered in the main text are based on non-saturating mass action but in this analysis we have included a more general saturating inhibition, which can be reduced to mass action in the limit of large $\hat{\rho}$ with $n = 1$. In the steady-state we find,

$$\hat{Y} = \frac{(\lambda\hat{C}_1 + \gamma_+^P)(\frac{1}{\hat{P}} - 1) - \gamma_-^P}{\hat{\beta_-^Y}}$$

which, we substitute into the steady-state of equation (2) to obtain,

$$f = 1 - \left[1 + \frac{\gamma_-^Y}{\frac{\eta_+^P}{1+\left(\frac{\hat{\rho}}{\hat{P}}\right)^n} + \gamma_+^Y}\right]\left[\frac{\kappa(\frac{1}{\hat{P}} - 1) - \gamma_-^P}{\hat{\beta_-^Y}}\right] = 0 \tag{4}$$

where $\kappa = \lambda\hat{C}_1 + \gamma_+^P$ contains the input from $\hat{C}_1$. To determine if P can exhibit a bell-shaped dose-response as a function of $\hat{C}_1$ we determine the value of the parameters where the first derivative of P is zero. To do this, we differentiate P with respect to κ,

$$\frac{\mathrm{d}f}{\mathrm{d}\kappa} = -\left[\frac{-n\gamma_-^Y\eta_+^P\left(\frac{\hat{\rho}}{\hat{P}}\right)^n\frac{\mathrm{d}\hat{P}}{\mathrm{d}\kappa}}{\hat{P}\left(\frac{\eta_+^P}{1+\left(\frac{\hat{\rho}}{\hat{P}}\right)^n} + \gamma_+^Y\right)^2\left[1+\left(\frac{\hat{\rho}}{\hat{P}}\right)\right]^2}\right]\left[\frac{\kappa(\frac{1}{\hat{P}} - 1) - \gamma_-^P}{\hat{\beta_-^Y}}\right]$$
$$- \left[1 + \frac{\gamma_-^Y}{\frac{\eta_+^P}{1+\left(\frac{\hat{\rho}}{\hat{P}}\right)^n} + \gamma_+^Y}\right]\left[\frac{1}{\hat{\beta_-^Y}}\left(\frac{\hat{P} - \kappa\frac{\mathrm{d}\hat{P}}{\mathrm{d}\kappa}}{\hat{P}^2} - 1\right)\right] = 0 \tag{5}$$

At $\frac{\mathrm{d}\hat{P}}{\mathrm{d}\kappa} = 0$, equation (5) reduces to

$$-\left[1 + \frac{\gamma_-^Y}{\frac{\eta_+^P}{1+\left(\frac{\hat{\rho}}{\hat{P}}\right)^n} + \gamma_+^Y}\right]\left[\frac{1}{\hat{\beta_-^Y}}\left(\frac{1}{\hat{P}} - 1\right)\right] = 0$$

which can be satisfied when

$$1 + \frac{\gamma_-^Y}{\frac{\eta_+^P}{1+\left(\frac{\hat{\rho}}{\hat{P}}\right)^n} + \gamma_+^Y} = 0 \tag{6}$$

and/or when

$$\frac{1}{\hat{\beta_-^Y}}\left(\frac{1}{\hat{P}} - 1\right) = 0 \tag{7}$$

Given that all reaction rate constants and concentrations must be positive it is clear that there are no values of $\hat{P}$ and reaction rate constants that satisfy equation (6). We do find that equation (7) can be satisfied when $\hat{P} = 1$ (i.e. $\hat{P}$ is maximally active) but at this value of $\hat{P}$ we find that the equation for f,

$$f = 1 + \frac{\gamma_-^P}{\hat{\beta_-^Y}}\left[1 + \frac{\gamma_-^Y}{\frac{\eta_+^P}{1+\hat{\rho}^n} + \gamma_+^Y}\right] = 0$$

which, as above, can never be realised because all reaction rates must be equal or greater than zero. Therefore, we conclude that a simple negative feedback motif cannot explain the observed optimum in the dose-response curve.

We have also performed this analysis on a 3 node network with non-saturating mass action (Figure S 5d-f). As before, C_1 activates P which in this network indirectly activates the inhibitor X by the activation of Y. In this architecture we observe oscillations in time (Figure S5e) but a bell-shaped dose-response in the steady state was not possible (Figure S5f). In what follows we show that this model is a special case of the model presented above and in this way we show that it cannot produce bell-shaped dose-response curves.

The system of ODEs for this model are,

$$\frac{\mathrm{d}\hat{X}}{\mathrm{d}t} = \hat{\eta_+^Y}\hat{Y}(1-\hat{X}) + \gamma_+^X(1-\hat{X}) - \gamma_-^X\hat{X} \tag{8}$$

$$\frac{\mathrm{d}\hat{P}}{\mathrm{d}t} = (\lambda\hat{C_1} + \gamma_+^P)(1-\hat{P}) - \gamma_-^P\hat{P} - \hat{\beta_-^X}\hat{X}\hat{P} \tag{9}$$

$$\frac{\mathrm{d}\hat{Y}}{\mathrm{d}t} = (\hat{\delta_+^P}\hat{P} + \gamma_+^Y)(1-\hat{Y}) - \gamma_-^Y\hat{Y} \tag{10}$$

where $\hat{X} = \frac{X}{X_T}$, $\hat{P} = \frac{P}{P_T}$, $\hat{Y} = \frac{Y}{Y_T}$, $\hat{\eta_+^Y} = \eta_+^Y Y_T$, $\hat{\beta_-^X} = \beta_-^X X_T$ and $\hat{\delta_+^P} = \delta_+^P P_T$. In the steady-state we find,

$$\hat{X} = \frac{(\lambda\hat{C_1}+\gamma_+^P)(\frac{1}{\hat{P}}-1)-\gamma_-^P}{\hat{\beta_-^X}}$$

$$\hat{Y} = \frac{1}{1+\frac{\gamma_-^Y}{\hat{\delta_+^P}\hat{P}+\gamma_+^Y}} \quad ,$$

which can be substituted into the steady-state expression for $\frac{\mathrm{d}\hat{X}}{\mathrm{d}t}$ to obtain an implicit equation for $\hat{P}$ in terms of the parameters of the system,

$$g = 1 - \left[1 + \frac{\gamma_-^X}{\frac{\eta_+^{\hat{Y}}}{1+\frac{\gamma_-^Y}{\delta_+^{\hat{P}}\hat{P}+\gamma_+^Y}} + \gamma_+^X}\right]\left[\frac{\kappa\left(\frac{1}{\hat{P}} - 1\right) - \gamma_-^P}{\beta_-^{\hat{X}}}\right] = 0 \tag{11}$$

where again, $\kappa = \lambda\hat{C}_1 + \gamma_+^P$. When $n = 1$ the equation for f (derived above) is identical to the equation of g with the exception of a constant. Given that the conclusions above are independent of n it follows that we can conclude that this 3 node network with negative feedback cannot exhibit bell-shaped dose-response curves in the steady-state. This is consistent with results from the systematic network analysis that did not find any negative feedback networks compatible with the phenotypic features.

Predicted T cell activation by co-presentation of pMHC ligands in the KPL-IFF model

The KPL-IFF model was extended to include an additional pMHC by first calculating the fraction of TCR bound to each ligand at steady-state using the following set of coupled ODEs,

$$\begin{aligned}
\mathrm{d}L^1/\mathrm{d}t &= -k_{\text{on}}^1 L^1 R + k_{\text{off}}^1 C^1 \\
\mathrm{d}L^2/\mathrm{d}t &= -k_{\text{on}}^2 L^2 R + k_{\text{off}}^2 C^2 \\
\mathrm{d}R/\mathrm{d}t &= -k_{\text{on}}^1 L^1 R + k_{\text{off}}^1 C^1 - k_{\text{on}}^2 L^2 R + k_{\text{off}}^2 C^2 \\
\mathrm{d}C^1/\mathrm{d}t &= k_{\text{on}}^1 L^1 R - k_{\text{off}}^1 C^1 \\
\mathrm{d}C^2/\mathrm{d}t &= k_{\text{on}}^2 L^2 R - k_{\text{off}}^2 C^2
\end{aligned}$$

where C^1 and C^2 are the concentration of TCR bound to the first and second pMHC ligands. These ODEs were integrated to the steady-state to determine C^1 and C^2, which were used to calculate P as follows,

$$\begin{aligned}
\hat{C}_1^1 &= \left(\frac{k_{\text{off}}^1}{k_{\text{off}}^1 + k_{\text{p}}}\right)\left(\frac{k_{\text{p}}}{k_{\text{off}}^1 + \phi k_{\text{p}}}\right)\hat{C}^1 \\
\hat{C}_1^2 &= \left(\frac{k_{\text{off}}^2}{k_{\text{off}}^2 + k_{\text{p}}}\right)\left(\frac{k_{\text{p}}}{k_{\text{off}}^2 + \phi k_{\text{p}}}\right)\hat{C}^2 \\
\hat{Y} &= \frac{1 + \hat{\lambda}(\hat{C}_1^1 + \hat{C}_1^2)}{1 + \hat{\lambda}(\hat{C}_1^1 + \hat{C}_1^2) + \hat{\gamma}^y} \\
\hat{P} &= \frac{1 + \hat{\delta}\hat{Y}}{1 + \hat{\delta}\hat{Y} + \hat{\gamma}^p + \hat{\mu}(\hat{C}_1^1 + \hat{C}_1^2)}
\end{aligned}$$

where superscripts indicate ligand identity (1 or 2). Parameter values are identical to those used to generate Figure 3d with the ligand concentration and kinetic parameters as indicated in Figure 5.

Model of kinetic proofreading with limited signalling followed by TCR internalisation

The following ODEs were used to model kinetic proofreading with limited signalling with constitutive and induced TCR internalisation,

$$\begin{aligned}
\mathrm{d}L/\mathrm{d}t &= -k_{\mathrm{on}}LR + k_{\mathrm{off}}(C_0 + C_1 + C_2) + \beta(C_0 + C_1 + C_2) \\
\mathrm{d}R/\mathrm{d}t &= -k_{\mathrm{on}}LR + k_{\mathrm{off}}(C_0 + C_1) + \alpha - \beta R \\
\mathrm{d}C_0/\mathrm{d}t &= k_{\mathrm{on}}LR - (k_{\mathrm{off}} + k_{\mathrm{p}} + \beta)C_0 \\
\mathrm{d}C_1/\mathrm{d}t &= k_{\mathrm{p}}C_0 - (k_{\mathrm{off}} + \phi k_{\mathrm{p}} + \beta)C_1 \\
\mathrm{d}C_2/\mathrm{d}t &= \phi k_{\mathrm{p}}C_1 - (k_{\mathrm{off}} + \beta)C_2
\end{aligned}$$

where α and β are the constitutive receptor recycling rates. In this model, it is assumed that C_2 represents a state where the receptor is tagged for induced internalisation so that immediately upon pMHC unbinding it is internalised (i.e. $k_{\mathrm{off}}C_2$ does not appear in the equation for R). The model is integrated to the steady-state using the Matlab (Mathworks, MA) function *ode23s* with the parameters indicated in Figure S8.

Supplementary Movies

Movie S1. Systematic analysis of 304 network architectures (Figure 4a). Each 1 second frame shows the network architecture (left) and the network output (right). The network architecture displays the 3 receptor states (C_0, C_1, and C_2) together with Y and P where green arrows indicate activation and red arrows indicate inhibition (magnitudes of inhibition arrows are in italics). The network output displays P (y-axis) over the ligand concentration (x-axis) for ligands with decreasing k_{off} (blue to red). Networks appear in ascending order of the SSR with networks that are better able to produce the phenotypic features appearing first. See Supplementary Information for computational details.

Movie S2. Systematic analysis of 26,069 network architectures (Figure 4e). Movie generated as described (see Movie S1) except that one additional receptor state and one additional node were included (see main text and Figure 4e for details). This movie can be found at this link: https://dx.doi.org/10.6084/m9.figshare.3491792.v1

Supplementary Applet

Applet S1. A Javascript applet that can be used to examine how the 5 model parameters (k_{p}, ϕ, μ, λ, and δ) modulate the predicted dose-response for ligands of varying affinities for the KPL-IFF model (Figure 3d). Default parameter values in the applet are the same as those used to generate Fig. 3d. This applet can be found at this link: https://dx.doi.org/10.6084/m9.figshare.3491807.v1

Supplementary Table

pMHC	Peptide	k_{off} (s^{-1})	SEM	k_{on} ($M^{-1}s^{-1}$)	SEM	K_D (M)	SEM
9V	SLLMWITQV	8.26E-05	1.03E-06	1.17E+06	2.80E+04	7.07E-11	2.57E-12
4A	SLLAWITQV	1.54E-03	1.77E-05	1.41E+06	1.15E+05	1.09E-09	1.01E-10
5Y	SLLMYITQV	1.67E-03	1.18E-04	1.26E+06	3.14E+05	1.33E-09	4.26E-10
8S	SLLMWITSV	1.33E-02	2.29E-03	1.03E+06	2.72E+05	1.29E-08	5.64E-09
6T	SLLMWTTQV	7.14E-02	1.43E-02	8.64E+05	2.70E+05	8.27E-08	3.58E-08
5F	SLLMFITQV	1.01E-01	7.08E-03	1.09E+06	2.03E+05	9.31E-08	2.39E-08
8K	SLLMWITKV	8.33E-02	6.46E-03	4.10E+05	2.98E+04	2.03E-07	3.05E-08
5P	SLLMPITQV	9.80E-01	7.76E-02	2.02E+06	2.39E+05	4.85E-07	9.59E-08
4A8K	SLLAWITKV	1.95E+00	5.31E-02	1.10E+06	1.34E+05	1.78E-06	2.65E-07
4A5A	SLLAAITQV	5.64E+00	5.62E-01	2.52E+05	5.47E+04	2.24E-05	7.10E-06
4A5P8K	SLLAPITKV					>1.0E-04	

Table S 1: Measured binding properties for the c58c61 TCR for the indicated peptide in complex with HLA-A*02:01 (pMHC ligand). Results are averages of at least 3 measurements.

Supplementary Figures

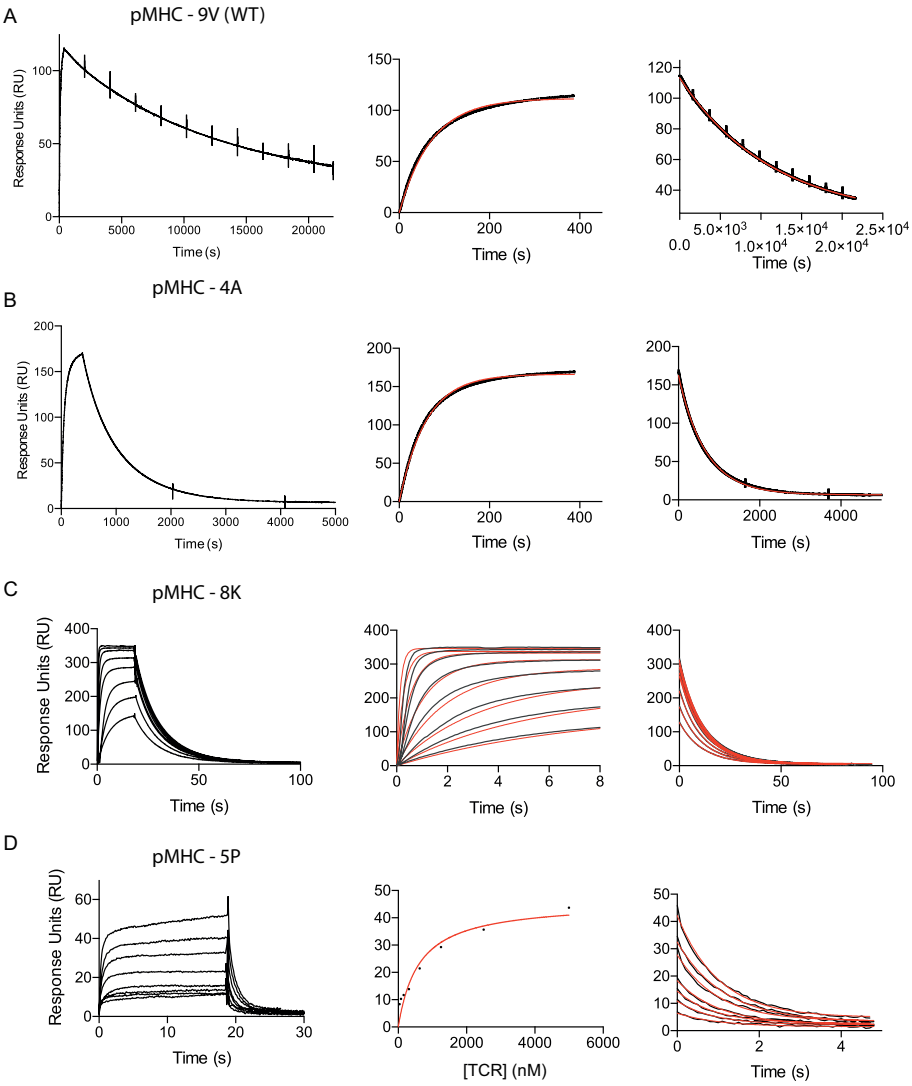

Figure S1: Representative surface plasmon resonance (SPR) measurements of TCR-pMHC interactions (Table S1). All experiments are performed by injecting recombinant c58c61 TCR over immobilised recombinant pMHC (see Materials & Methods). The precise protocol for determining the kinetic rate constants (k_{on} and k_{off}) was dependent upon the affinity regime of the TCR-pMHC interaction. a-b) In the case of TCR-pMHC interaction with small k_{off}, a single concentration of TCR is injected over the surface. The value of k_{off} is determined from the dissociation curve (right) which is used to fit the association curve (middle) with exponential rate of $k_{\text{on}}[\text{TCR}]+k_{\text{off}}$. c-d) In the case of TCR-pMHC interactions with a larger k_{off}, multiple concentrations of the TCR were injected over the surface. The value of k_{off} was determined from the dissociation curve and the value of k_{on} was either determined from fitting the association curves (as in c) or by first determining the K_{D} ($k_{\text{on}} = k_{\text{off}}/K_{\text{D}}$, as in d). When kinetics were too rapid to be resolved we only report the value of K_{D}. See Materials & Methods for a detailed protocol and mathematical analysis of the data.

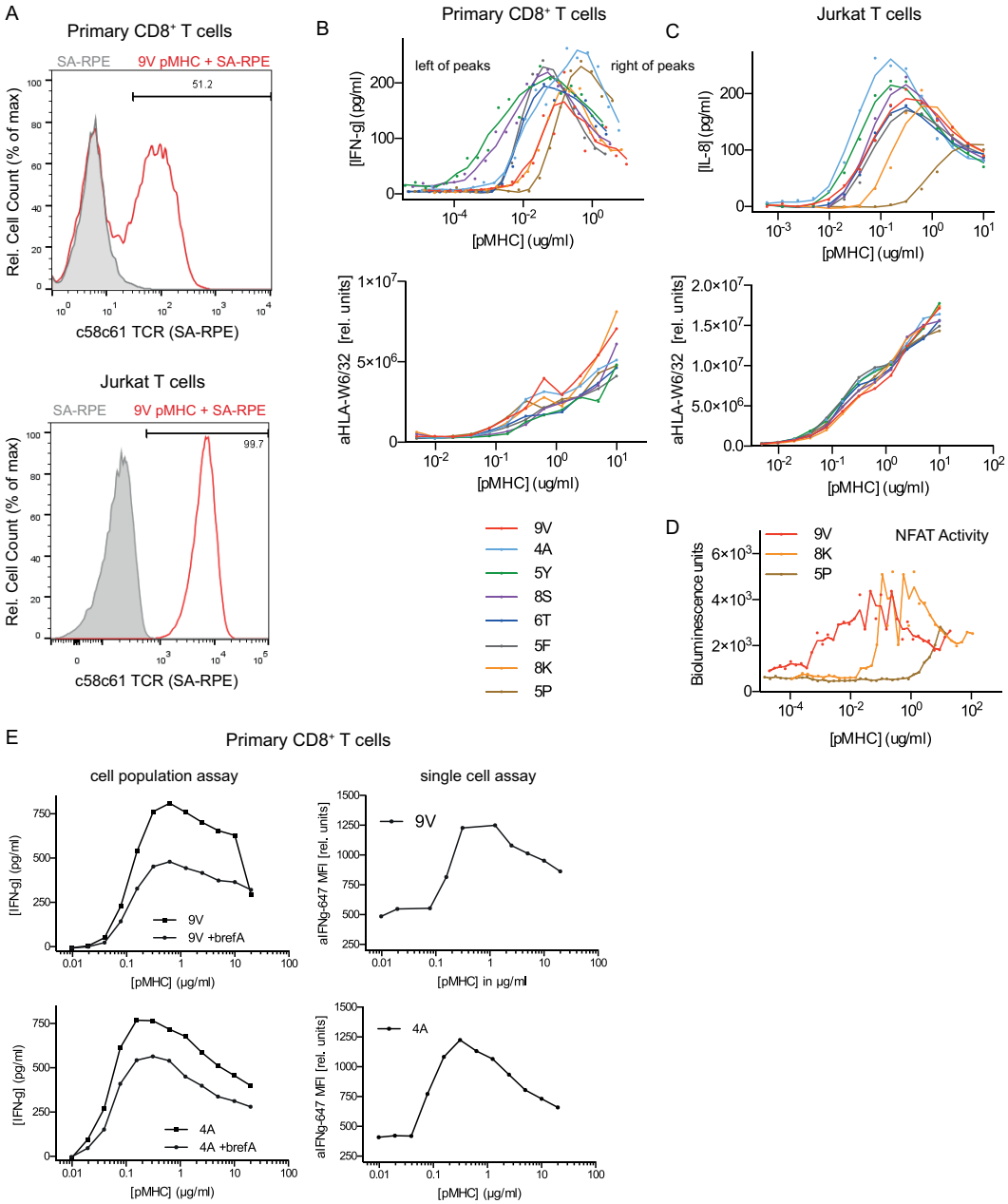

Figure S2: a) Expression of the c58c61 TCR on primary CD8$^+$ T cells and Jurkat T cells using the biotinylated high affinity pMHC (9V) with R-PE-conjugated streptavidin (red line) or only R-PE-conjugated streptavidin as a staining control (grey line). The Jurkat T cells were sorted following transduction. b,c) Functional assays (top) together with pMHC immobilisation controls (bottom) for b) primary CD8$^+$ T cells and c) Jurkat T cells with a larger number of higher affinity ligands. Functional assays were corrected for differences in pMHC immobilisation (see Materials & Methods). d) The transcriptional activity of NFAT in Jurkat T cells was determined at 16 hours for the indicated pMHC ligands revealing qualitatively similar behaviour to IL-8. This reporter of T cell activation was not used routinely because of the poor signal-to-noise ratio of the assay. e) Activation assays with primary T cells were performed as described in the main text for the indicated pMHC except that brefeldin A was added to block cytokine secretion for the last 2 hours of the assay (reducing the amount of supernatant cytokine in the cell population assay, left column) at which point intracellular cytokine levels were determined by flow cytometery (right column). The supernatant concentration of cytokine (cell population assay) compares favorably with the mean intensity of cytokine in the positive population (single cell assay). All data are representative of at least 3 independent experiments.

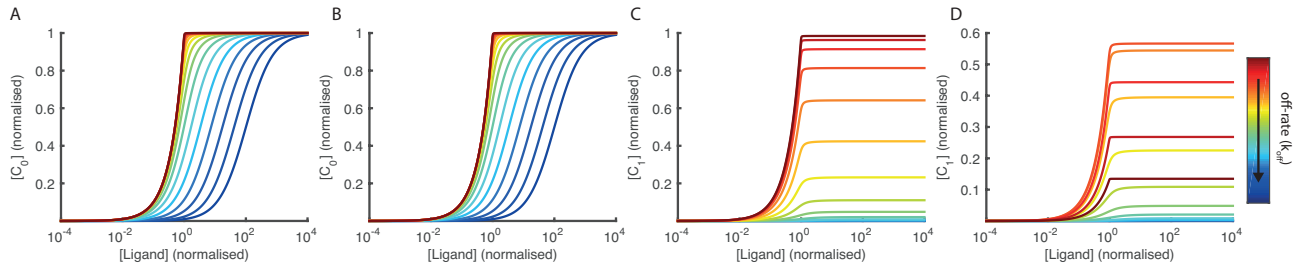

Figure S3: The concentration of TCR-pMHC complexes that regulate the activation of P for the phenotypic model calculations in Figure 3. The concentration of a) C_0 in the occupancy model, b) C_0 in the occupancy coupled to incoherent feedforward model, c) C_1 in the kinetic proofreading coupled to incoherent feedforward model, and d) C_1 in the KPL-IFF model. The the maximum concentration of signalling competent TCR-pMHC complexes for the occupancy models (a,b) is independent of the TCR-pMHC off-rate (k_{off}) whereas for the kinetic proofreading models (c,d) the maximum concentration of signalling competent TCR-pMHC complexes is dependent on the off-rate.

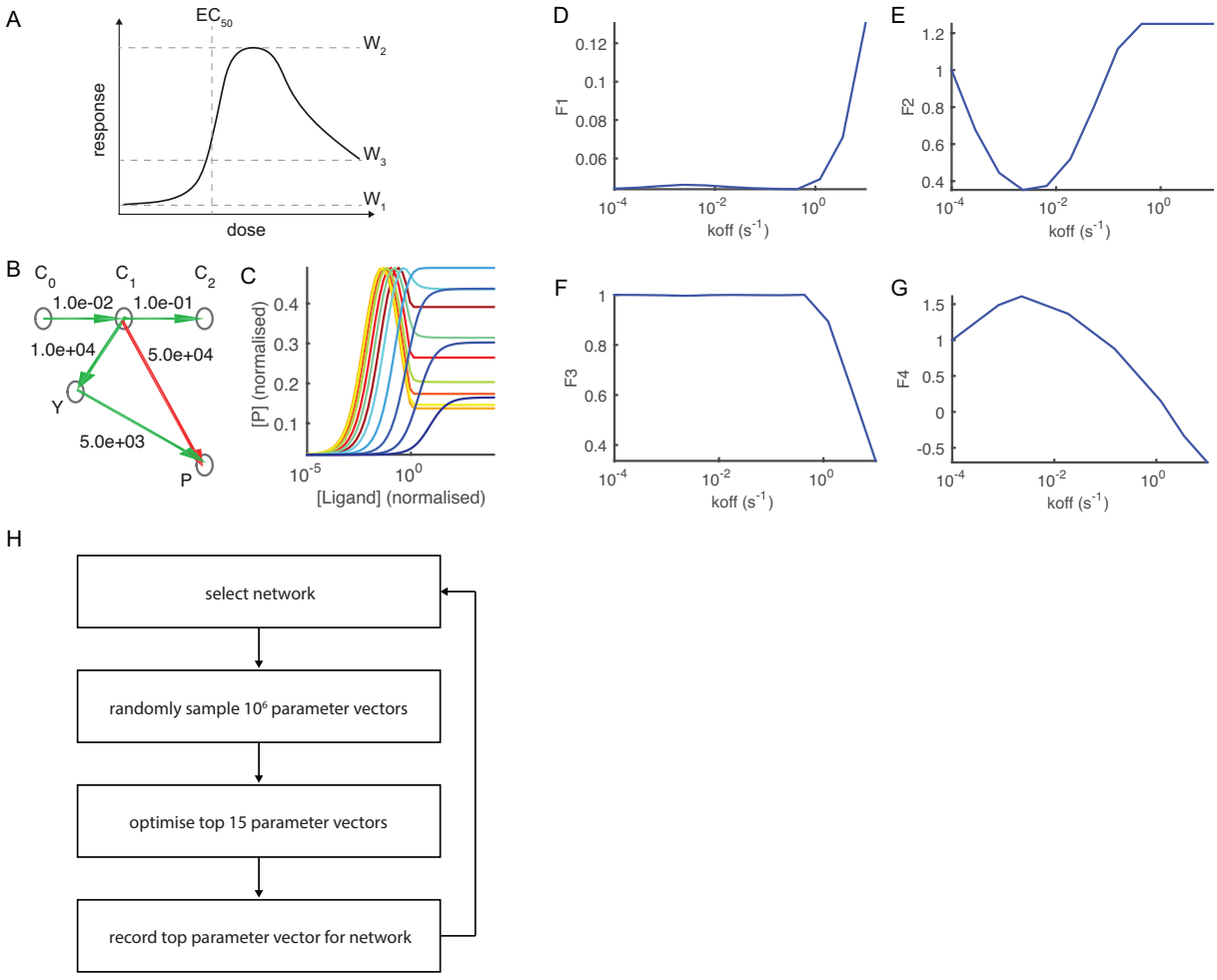

Figure S4: Quantitative metrics for comparing signalling network outputs. a) Schematic of a bell-shaped dose-response showing the definition of W_1, W_2, W_3, and EC_{50}. b) Schematic of the network architecture of the KPL-IFF phenotypic model where green arrows indicate activation and red arrows indicate inhibition with the magnitude of the arrow indicated (compare to Figure 3d). d) Output of the KPL-IFF phenotypic model shown in B with 12 pMHC ligands whose k_{off} varies from 10^{-4} (red) to 10 (blue). d-g) The values of the metrics F_1, F_2, F_3, and F_4 as a function of k_{off} for the output in panel c. h) Workflow of the systematic network search algorithm.

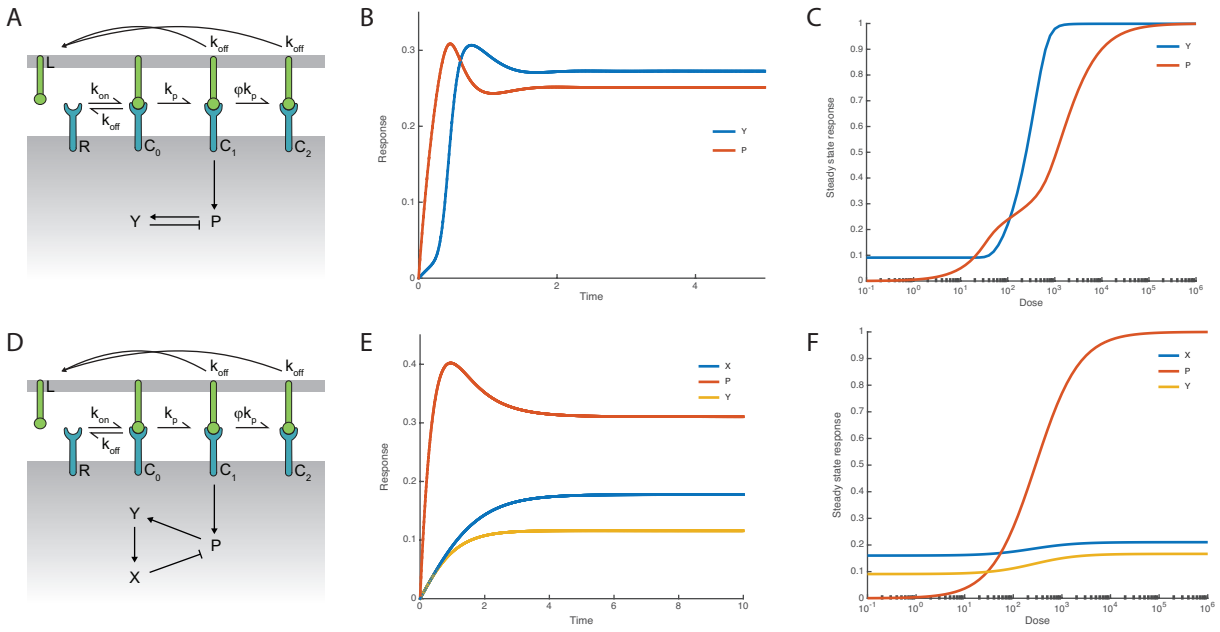

Figure S5: Negative feedback can produce oscillations in time but not bell-shaped dose-response curves in the steady-state. a) A two node negative feedback, whereby P activates its inhibitor Y (see Figure 4d) can b) produce oscillations in P over time but c) not bell-shaped dose-response in the steady-state. d) A three node negative feedback, where P activates Y which in turn activates X that is able to inhibit P can (as for the two component negative feedback) e) produce damped oscillations in P over time but f) not bell-shaped dose-response in the steady-state. See Supplementary Information for calculation details.

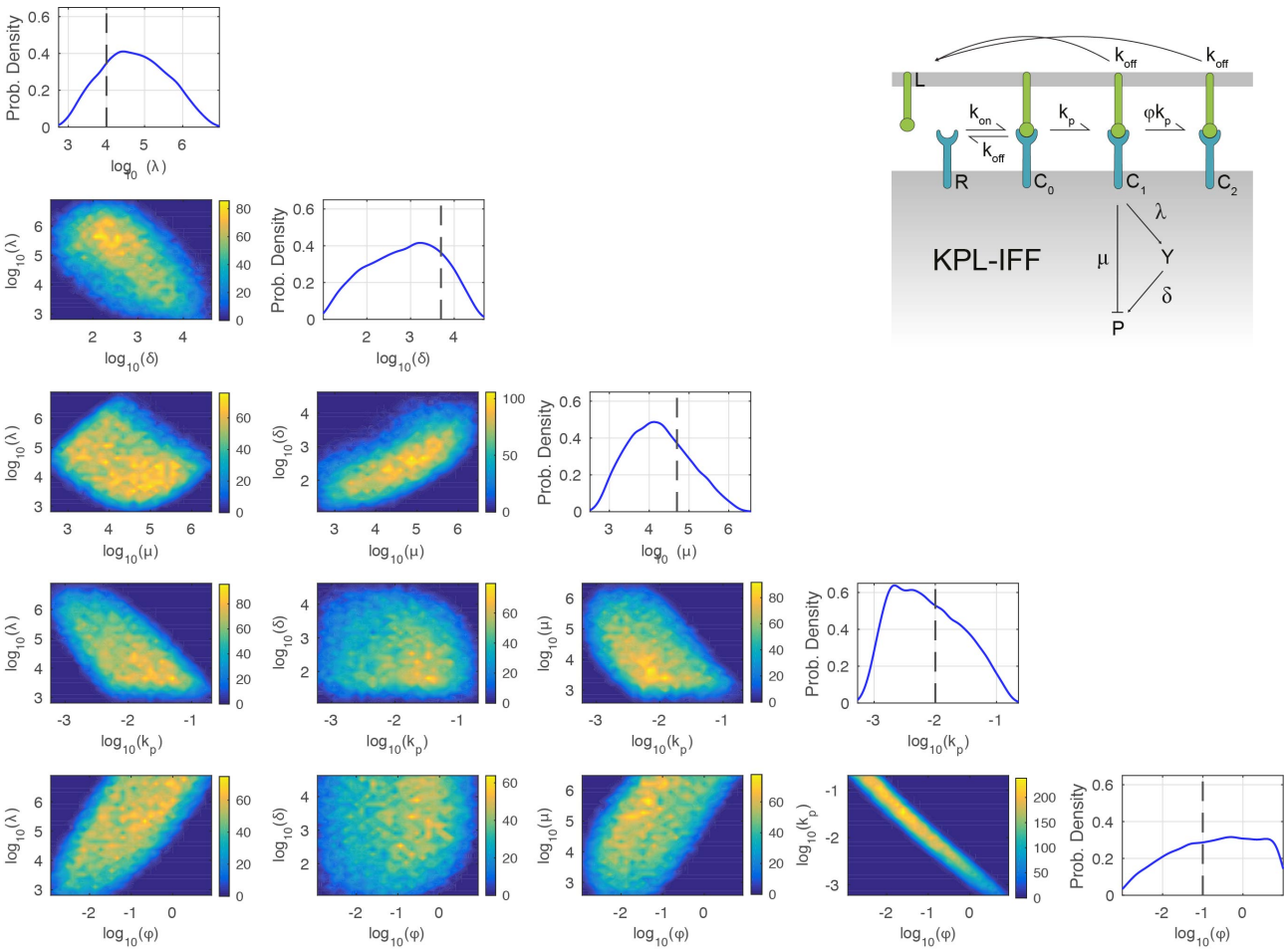

Figure S6: KPL-IFF model parameters compatible with phenotypic features. The probability density of the indicated parameter is shown along the diagonal along with pairwise correlations in the off-diagonals with yellow indicating a high frequency of occurence (scale bar indicates number of occurrences). Vertical dashed lines in the probability densities indicate the default parameter used in Figure 3d. We find a broad range of parameter values compatible with phenotypic features but with certain relationships amongst them. For example, we find that $\mu > \delta$ but both parameters can vary more than 1000-fold provided this relationship is maintained. See Supplementary Information for calculation details.

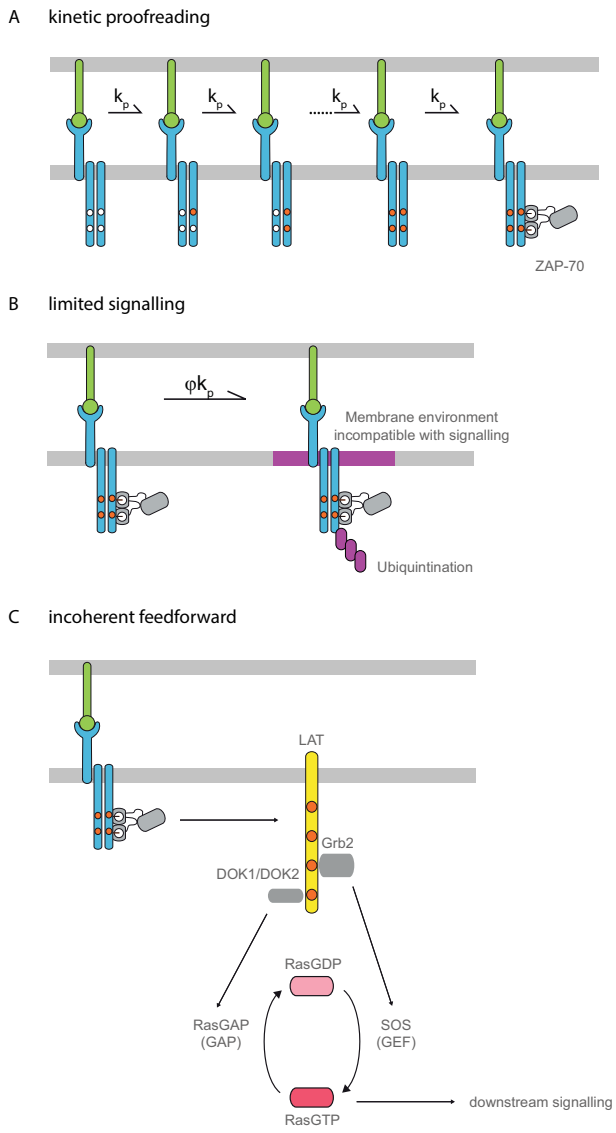

Figure S7: Possible relationships between the phenotypic model modules and known T cell signalling components. a) Kinetic proofreading can be realised by the sequential phosphorylation of the T cell receptor ITAMs and/or the recruitment of Lck associated coreceptors (5) (not shown) followed by the recruitment and subsequent activation of ZAP-70 (6) . b) Limited signalling of the T cell receptor may occur as a result of ubiquintination (7) and/or the receptor entering membrane environments that are incompatible with signalling (8). c) Incoherent feedforward in the signalling cascade initiated by the T cell receptor may occur between LAT and Ras (9). Phosphorylated LAT provides docking sites for Grb2 which recruits the guanine nucleotide exchange factor (GEF) SOS that promotes the formation of the active form of Ras (RasGTP) that promotes downstream signalling. However, phosphorylated LAT also provides docking sites for DOK1/DOK2 which recruits the GTPase activating protein (GAP) RasGAP that promotes the formation of RasGDP and hence reduces the active form of Ras. Although not depicted in the schematic, incoherent feedforward may also arise from the TCR signalosome because it is able to associate with both a tyrosine kinase (ZAP-70) and a tyrosine phosphatase (SHP-1) (10).

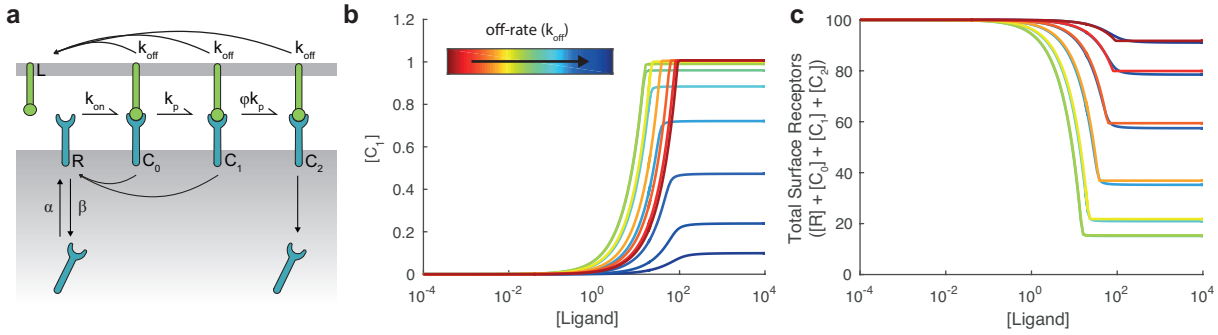

Figure S8: Internalisation of TCR following signalling does not produce bell-shaped dose-responses in the steady-state. a) Schematic of internalisation model that includes kinetic proofreading with limited signalling followed by TCR internalisation (from state C_2) with basal recycling of receptor at the cell surface. b) Concentration of signalling TCR and c) total surface TCR over ligand concentrations for different ligand affinities at steady-state. Parameters: $k_{\mathrm{p}} = 0.01\ \mathrm{s}^{-1}$, $\phi = 0.1$, $\alpha = 0.01\ \mu\mathrm{m}^{-2}\mathrm{s}^{-1}$, $\beta = 0.001\ \mathrm{s}^{-1}$ with a variation of k_{off} from 10^{-4} to 10^{2} s^{-1} (coloured lines).

References

1. Ma W, Trusina A, El-Samad H, Lim Wa, Tang C (2009) Defining network topologies that can achieve biochemical adaptation. *Cell* 138:760–73.

2. Shah Na, Sarkar Ca (2011) Robust network topologies for generating switch-like cellular responses. *PLoS Computational Biology* 7.

3. Toni T, Welch D, Strelkowa N, Ipsen a, Stumpf MP (2009) Approximate Bayesian computation scheme for parameter inference and model selection in dynamical systems. *Journal of The Royal Society Interface* 6:187–202.

4. Sunnåker M, et al. (2013) Approximate bayesian computation. *PLoS computational biology* 9:e1002803.

5. Stepanek O, et al. (2014) Coreceptor Scanning by the T Cell Receptor Provides a Mechanism for T Cell Tolerance. *Cell* 159:333–345.

6. Acuto O, Di Bartolo V, Michel F (2008) Tailoring T-cell receptor signals by proximal negative feedback mechanisms. *Nature Reviews Immunology* 8:699–712.

7. Yang M, et al. (2015) K33-linked polyubiquitination of Zap70 by Nrdp1 controls CD8+ T cell activation. *Nature Immunology* 16:1–12.

8. Choudhuri K, et al. (2014) Polarized release of T-cell-receptor-enriched microvesicles at the immunological synapse. *Nature* 507:118–123.

9. Brownlie RJ, Zamoyska R (2013) T cell receptor signalling networks: branched, diversified and bounded. *Nature Reviews Immunology* 13:257–269.

10. Altan-Bonnet G, Germain RN (2005) Modeling T cell antigen discrimination based on feedback control of digital ERK responses. *PLoS biology* 3:e356.